HHS Public Access
Author manuscript
Magn Reson Med. Author manuscript; available in PMC 2019 July 01.

Published in final edited form as:
Magn Reson Med. 2018 July ; 80(1): 190–199. doi:10.1002/mrm.27025.

A Rapid T_1 Mapping Method for Assessment of Murine Kidney Viability Using Dynamic Manganese-Enhanced Magnetic Resonance Imaging

Kai Jiang, PhD[1], **Hui Tang, PhD**[1], **Prassana K. Mishra, PhD**[2], **Slobodan I. Macura, PhD**[2], and **Lilach O. Lerman, MD, PhD**[1]

[1]Division of Nephrology and Hypertension, Mayo Clinic, Rochester, Minnesota, USA

[2]Biochemistry and Molecular Biology, Mayo Clinic, Rochester, Minnesota, USA

Abstract

Purpose—Dynamic manganese-enhanced MRI (MEMRI) allows assessment of tissue viability by tracing manganese uptake. We aimed to develop a rapid T_1 mapping method for dynamic MEMRI to facilitate assessments of murine kidney viability.

Methods—A multi-slice saturation recovery fast spin echo (MSRFSE) was developed, validated, and subsequently applied in dynamic MEMRI at 16.4 T on ischemic mouse kidneys after 4 weeks of unilateral renal artery stenosis (RAS). Baseline T_1 values and post-contrast R_1 ($1/T_1$) changes were measured in cortex (CO), outer (OSOM), inner (ISOM) strips of outer medulla, and inner medulla (IM).

Results—Validation studies showed strong agreement between MSRFSE and an established saturation recovery Look-Locker method. Baseline T_1 (s) increased in the stenotic kidney CO (2.10 (1.95–2.56) vs. 1.88 (1.81–2.00), P=0.0317) and OSOM (2.17 (2.05–2.33) vs. 1.96 (1.87–2.00), P=0.0075), but remained unchanged in ISOM and IM. This method allowed a temporal resolution of 1.43 min in dynamic MEMRI. Mn^{2+} uptake and retention decreased in stenotic kidneys, particularly in the OSOM (ΔR_1: 0.48 (0.38–0.56) vs. 0.64 (0.61–0.69) s^{-1}, P<0.0001).

Conclusion—Dynamic MEMRI by MSRFSE detected decreased cellular viability and discerned the regional responses to RAS. This technique may provide a valuable tool for noninvasive evaluation of renal viability.

Keywords

Manganese-enhanced MRI; T_1 mapping; Kidney viability; Renal artery stenosis

*Address correspondence to: Lilach O. Lerman, MD, Ph.D., Division of Nephrology and Hypertension, Mayo Clinic, 200 First St SW, Rochester, MN 55905, Tel: (507)266-9376 Fax: (507)266-9316, Lerman.Lilach@mayo.edu.

DISCLOSURES of CONFLICTS of INTEREST
None.

INTRODUCTION

Divalent manganese ion (Mn^{2+}) is paramagnetic and constitutes a useful contrast agent in magnetic resonance imaging (MRI) due to its T_1 and T_2 shortening effects (1–3). Unlike gadolinium-based extracellular contrast agents, Mn^{2+}, as a calcium (Ca^{2+}) analog, can enter excitable cells via voltage-gated Ca^{2+} channels (4–6). Intracellular Mn^{2+} has a long half-life, due to its slow clearance and uptake by mitochondria (7). Since uptake and accumulation of Mn^{2+} in cells are largely dependent on cellular activity and metabolism, manganese-enhanced MRI (MEMRI) has been used to assess tissue viability or functionality in the heart (8, 9), pancreatic β-cells (10), and stem cells (11). The uptake and retention of Mn^{2+} has also been long recognized in the kidney (12), but the capability of MEMRI in assessing kidney viability has not been demonstrated.

Dynamic MEMRI using fast T_1-weighted imaging (13) or T_1 mapping (14–16) can be used to track the kinetics of Mn^{2+} uptake in tissue. Compared to T_1-weighed imaging, T_1 mapping allows more quantitative assessments of Mn^{2+} uptake in cells, because of the linear relationship between the longitudinal relaxation rate R_1 ($1/T_1$) and Mn^{2+} concentration (16, 17). At high or ultrahigh magnetic fields, T_1 mapping is typically achieved by tracking the dynamic recovery of longitudinal magnetization after either inversion or saturation, to eliminate the effect of B_1 inhomogeneity (18). While inversion recovery-based T_1 mapping methods provide excellent T_1 maps, they are somewhat slow due to long sequence repetition time. In comparison, saturation recovery-based T_1 mapping methods do not require full recovery of longitudinal magnetization, and thus allow rapid T_1 mapping.

Previously, a multi-slice saturation recovery Look-Locker (MSRLL) method was developed for fast (within 3 min) T_1 mapping in the mouse myocardium (16, 18). However, due to the low flip angle (10°) and small dynamic range for T_1 fitting, this method has limited signal-to-noise ratio (SNR). Compared to the Look-Locker data acquisition, fast spin echo (FSE) imaging provides higher SNR and is free from magnetic susceptibility-induced artifacts for body imaging, especially at high or ultrahigh magnetic fields (19). Importantly, the relatively stationary kidney allows implementation of FSE readout during image acquisition. Therefore, a saturation recovery FSE method may provide rapid and accurate T_1 mapping in the kidney.

In this study, we aimed to develop a multi-slice saturation recovery fast spin echo (MSRFSE) method for rapid T_1 mapping of murine kidneys at 16.4 T, to facilitate dynamic MEMRI in the kidney. This method was first validated both in vitro and in vivo by comparing to the previously established MSRLL method, and subsequently applied to monitor renal Mn^{2+} uptake in a murine model of unilateral renal artery stenosis (RAS), which induces ischemic renal injury and decreases cellular viability. We hypothesized that the dynamic MEMRI with the aid of MSRFSE might enable noninvasive assessment of renal viability.

METHODS

Imaging Method

The sequence diagram of MSRFSE comprised of three different segments: saturation, recovery, and fast spin echo readout. Whole-body magnetization saturation was achieved by using three 0.1-ms nonselective 90° hard pulses, each followed by spoil gradients (16, 18). Following varying time delays (TD), multiple lines in k-space from different slices were acquired with FSE readout. The echo train length (ETL) was set at eight, to balance image spatial resolution and acquisition time. A centric encoding scheme was implemented to achieve high SNR. T_1-weighted (M_t) and proton density (M_0) images were acquired for T_1 mapping. The TDs for M_t images were selected to cover the ascending portion of the magnetization recovery curve. For the M_0 image, a TD at 18s was used to ensure that the magnetization was at full equilibrium before image acquisition at 16.4 T.

Assuming a complete saturation of magnetization by the saturation module, the signal intensity in the MSRFSE-acquired images is governed by T_1 and T_2 given a specific set of TD and echo time (TE)

$$S(T_1, T_2) = S_0(1 - e^{-TD/T_1})e^{-TE/T_2} \quad [1]$$

where S_0 is a constant determined by proton density and the imaging system. With TD$\gg T_1$, signal intensity of the M_0 image can be simplified as:

$$S(T_2) = S_0 e^{-TE/T_2} \quad [2]$$

Using Taylor expansion, Eq. 2 can be written as:

$$S(T_2) = S_0\left(1 - TE/T_2 + \frac{(TE/T_2)^2}{2!} - \frac{(TE/T_2)^3}{3!} + \cdots\right) \quad [3]$$

If TE$\ll T_2$, Eq. 3 can be reduced to:

$$S(T_2) = S_0(1 - TE \cdot R_2) \quad [4]$$

where R_2 is equal to $1/T_2$. A slow infusion of $MnCl_2$ at low dose induces an approximately linear accumulation of Mn^{2+} and increase in R_2 over time (20). If the post-contrast kidney T_2 is still much larger than the effective TE, the M_0 image at a certain time point during $MnCl_2$ infusion can be linearly interpolated from two M_0 images acquired at baseline and post-contrast, respectively.

Phantom Study

All MRI studies were performed on a vertical 16.4 T animal scanner (Bruker, Billerica, MA) equipped with a 38mm inner diameter birdcage coil. The MSRFSE method was first validated by comparing to MSRLL in vitro using a multi-compartment $MnCl_2$ phantom with concentration ranging from 30 to 500 μM at room temperature. Seven M_t images of one slice were acquired with TD ranging from 0.2 to 2.0 s. Other imaging parameters were: FOV $3.0\times3.0cm^2$; matrix size 128×128; slice thickness 1.5mm; TD 0.2–2.0s; echo spacing 4.8ms; number of averages 1. An ETL of eight was found to provide acceptable image blurring as well as fast imaging, and was therefore subsequently applied in both the phantom and in vivo studies. The M_0 image was acquired with a TD of 18s. The acquisition times of M_t and M_0 images were 1.96 and 4.0 minutes, respectively. In MSRLL, a total of 20 Look-Locker images were acquired with a sampling interval of 200ms, a flip angle at 10°, and a single average. The central 64 lines were acquired in the phase encoding direction. The proton density image was acquired with repetition time at 3s. Other imaging parameters were the same as in the MSRFSE scan, for a total imaging time for the MSRLL method of 7.5 minutes.

Animal Study

This study was approved by the Institutional Animal Care and Use Committee. At the age of 3 months, fourteen 129S1 male mice (Jackson Lab, Bar Harbor, ME) underwent sham (n=7) or RAS (n=7) surgery, as described previously (21). Briefly, RAS was induced by placing a polytetrafluoroethylene tube (Braintree Scientific, Braintree, MA) around the right renal artery. Sham surgery included isolation of the renal artery, but without cuff placement. Four weeks later, mice were weighed and blood pressure measured by tail-cuff (XBP1000 system, Kent Scientific, Torrington, CT) prior to MRI.

Anesthesia was induced with 2% isoflurane in a mouse chamber and maintained with 1.0–2.0% during MRI. Mice were placed supine in a cradle, and kept vertical in the scanner. A homemade catheter with a needle size of 30G was secured in the mouse tail-vein for infusion of $MnCl_2$ solution. Warm air was blown to the mice to maintain the body temperature at ~36°C. Respiration and body temperature were monitored and recorded by a physiological monitoring system (SA Instruments, Stony Brook, NY).

The kidney volume was measured using a respiration-gated 3D Fast Imaging with Steady Precession sequence with the following parameters: TR 14ms; TE 2.7ms; flip-angle 20°; FOV $5.12\times2.56\times1.28$ cm^3; matrix size 256×128×64; number of averages 2. Images were acquired in the coronal plane.

In vivo dynamic MEMRI experiments by MSRFSE were conducted to evaluate the renal uptake of Mn^{2+} in RAS. Two slices located at the center of the two kidneys were imaged with a FOV $2.56\times2.56cm^2$. After baseline T_1 mapping, 16 mM $MnCl_2$ (Sigma Chemical Co., St Louis, MO) solution was infused through the tail vein catheter at a rate of 8 μl/g/hr for 15 minutes (32 nM/g BW), followed by a 15 minutes washout period. Six M_t images with TD from 0.2 to 1.5s were acquired repetitively and continuously during Mn^{2+} infusion and washout, resulting in a temporal resolution of 1.43 min for T_1 mapping. To account for signal intensity changes in the proton density-weighted images, M_0 images were acquired at both baseline and the end of the MEMRI study, with respiratory triggering prior to the FSE readout to reduce motion artifacts.

For in vivo validation of MSRFSE, T_1 maps of the same slices in the control mice were also measured using MSRLL at baseline and post-contrast. To increase SNR, two averages were used, with other imaging parameters the same as in the phantom study. The total imaging time for the MSRLL and MSRFSE methods in vivo were 14.94 and 5.96 minutes, respectively.

To evaluate Mn^{2+}-induced T_2 change, T_2 mapping was performed in all mice at baseline and post-contrast using a modified Carr–Purcell–Meiboom–Gill sequence (20). In this method, variable crusher gradients were applied before and after the 180° pulses to minimize the stimulated echo effects, and the slice thickness of the 180° pulses adjusted to three times of the excitation pulse to ensure a uniform refocusing across the imaging slice. The same two slices in the MEMRI study were imaged separately. Other imaging parameters were: FOV 2.56×2.56cm^2; matrix size 128×128; slice thickness 1.5mm; TR 500ms; echo spacing 6.0ms; number of echoes 10; number of averages 4. Respiratory triggering was applied to avoid motion artifacts.

To investigate the possible impact of changes in renal perfusion on measured R_1 during the MEMRI study, an additional group of control (n=3) and RAS (n=3) mice were infused with saline following the same protocol as in the MEMRI study. Dynamic T_1 changes in control (n=6), stenotic (n=3), and contralateral (n=3) kidneys were measured using MSRFSE during wash-in and washout.

Mice were euthanized immediately after the MEMRI experiment, and kidneys harvested for measurement of Mn concentration using inductively coupled plasma mass spectrometry (ICP-MS). Kidney samples were digested for 13 hours in 0.5 mL 70% trace metal grade nitric acid (Fisher Scientific, Fair Lawn, NJ) with the aid of heating at 120°C using a hot plate. Then, 0.2 mL 30% H_2O_2 were added for further digestion for 30 minutes, after which the solution was diluted to 20 mL using trace metal water (Fisher Scientific, Fair Lawn, NJ). Finally, 10 mL of each sample was used for measurement of Mn concentration using a Thermo Scientific iCAP Q ICP-MS instrument (Thermo Fisher Scientific GmbH, Bremen, Germany). In order to measure the Mn relaxivity in mouse kidneys at 16.4 T, the correlation between measured Mn concentration and ΔR_1 was assessed, after which the measured relaxivity was used for Mn content mapping using the pre- and post-contrast T_1 maps.

Image Analysis

Renal volumes were quantified using Analyze™ (version 12.0, Biomedical Imaging Resource, Mayo Clinic, MN), and all other images using in-house developed modules in Matlab® (Mathworks, Natick, MA). T_1 maps by MSRFSE were generated by mono-exponential curve fitting. All M_t images were normalized by the M_0 image, after which two unknown parameters, saturation efficiency (α) and T_1, were fitted using the trust-region-reflective algorithm by the following equation.

$$SI = (1 - \alpha)e^{-TD/T_1} + (1 - e^{-TD/T_1}) \quad [5]$$

where SI represents the normalized signal intensity with a maximal value of 1. While the TDs for the first slice were from 0.2 to 1.5 s, those for the second slice were adjusted by adding the delay (38.4 ms) induced by the FSE readout of the first slice. For MSRLL, all images were initially zero-filled to 128×128 during reconstruction, from which T_1 maps were generated using the method described previously (16).

In the phantom study, the T_1 relaxivity of Mn^{2+} in water was quantified by a simple linear correlation between the Mn^{2+} concentration ($[Mn^{2+}]$) and T_1 relaxation rate (R_1).

In the mouse study, M_t images (up to two) with severe motion artifacts were excluded before T_1 fitting. The proton density images at different time points during Mn^{2+} infusion were linearly interpolated using the two sets of M_0 images acquired at baseline and post-contrast. The post-contrast M_0 image was used for T_1 mapping during washout. A manual segmentation of kidney into cortex (CO), outer strip of outer medulla (OSOM), inner strip of outer medulla (ISOM), and inner medulla (IM) was performed on post-contrast T_1 maps, which showed a good contrast between different renal zones. Baseline MSRFSE-measured T_1 values in these zones were quantified and compared to those measured by MSRLL. Dynamic R_1 changes in CO, OSOM, ISOM, and IM during MEMRI were also measured, and the R_1 changes (ΔR_1) from baseline to post-Mn^{2+} infusion calculated and used to represent Mn^{2+} uptake. Similarly, dynamic R_1 changes in different regions of kidneys in the sham injection groups were measured.

T_2 maps were fitted pixel-wise according to the following equation, which contains three unknown parameters: the signal intensity with TE at zero S_0, T_2, and noise σ.

$$S(TE) = S_0 \cdot e^{-TE/T_2} + \sigma \quad [6]$$

Then T_2 values at CO, OSOM, and ISOM were quantified using the same ROIs manually traced on the T_1 maps.

Statistical Analysis

Statistical analysis was performed using JMP 10.0 (SAS Institute, Cary, NC). Normality of the data was assessed using the Shapiro-Wilk test and results expressed as means ± standard deviations for normally distributed data or medians with interquartile ranges for non-normally distributed data. For comparison between groups, one-way analysis of variance (ANOVA) followed by unpaired Student's t-test or the Wilcoxon rank-sum test, as appropriate. For comparison within groups, one-way ANOVA was followed by paired Student's t-test or the Wilcoxon signed-rank test, as appropriate. Bland-Altman analysis was performed to compare the T_1 values measured by MSRFSE and MSRLL in vivo. Two-way repeated measures ANOVA was performed to compare the time courses of R_1 changes of the control, stenotic, and contralateral kidneys.

RESULTS

Phantom Study

Representative M_t images acquired at different TDs and the M_0 image by MSRFSE are shown in Fig. 1a. Increasing $MnCl_2$ concentrations shortened T_1 and thus accelerated the magnetization recovery after saturation. The fitted T_1 maps by MSRFSE and MSRLL are shown in Fig. 1b. A strong agreement was observed in the measured T_1 values by these two methods at different $MnCl_2$ concentrations (Fig. 1c), indicating that the MSRFSE method provides an accurate measurement of T_1. A linear correlation between Mn^{2+} concentration and R_1 yielded a T_1 relaxivity of 6.16 s^{-1}/mM for Mn^{2+} in water at 16.4 T, slightly higher than obtained at 7 T (5.01 s^{-1}/mM) (16).

Animal Characteristics

At 4 weeks after surgery, RAS mice had similar body weight as the controls, but showed significantly elevated systolic, diastolic, and mean arterial pressures (Table 1). The stenotic kidney volume (176.9±17.3 μL) was decreased compared to control (284.9±44.5 μL, $P<0.001$) and contralateral (293.5±41.4 μL, $P<0.001$) kidneys, confirming a hemodynamically significant stenosis.

In Vivo T_1 Mapping by MSRFSE and Validation Study

Representative M_t images acquired at different TDs and the M_0 image of normal mouse kidneys are shown in Fig. 2a. With an ETL of 8, anatomical details can be observed in kidneys, despite slight image blurring. The good SNR (>80 in M_0 image) gave rise to robust mono-exponential T_1 fitting in individual pixels located in CO, OSOM, ISOM and IM (Fig. 2b). The fitted saturation efficiency and T_1 maps overlaid on the M_0 image are shown in Fig. 2c and d, respectively. Our saturation module offered a nearly complete saturation of longitudinal magnetization (>99%). T_1 values were larger in ISOM and IM, possibly due to accumulation of filtrate and urine in the renal tubules and collecting system.

Representative T_1 maps acquired by MSRFSE and MSRLL at pre- and post-Mn^{2+} infusion in control mice are shown in Fig. 3a. A good spatial agreement in T_1 maps by these two methods was observed. Slight difference between the two in post-contrast T_1 maps may be attributed to Mn^{2+} washout during T_1 mapping. Quantitative comparison showed no difference in T_1 measurements between MSRFSE and MSRLL methods either before or after $MnCl_2$ infusion (Fig. 3b). At baseline, the MSRFSE-measured T_1 values (in s) at different zones of the kidney were CO 1.94 ± 0.10, OSOM 2.02 ± 0.12, ISOM 2.37 ± 0.09, and IM 3.14 ± 0.07. After Mn^{2+} infusion, the T_1 values decreased to 1.06 ± 0.11, 0.99 ± 0.13, ISOM 1.25 ± 0.06, and IM 2.65 ± 0.21, respectively (all $P<0.001$). Bland-Altman analysis also showed strong agreement between T_1 values measured by MSRFSE and MSRLL (Fig. 3c) at both pre- and post-Mn^{2+} infusion.

T_2 at Pre- and Post-Mn^{2+} Infusion

Representative T_2 maps of the control, stenotic, and contralateral kidneys are shown in Fig. 4a. At baseline, the measured T_2 values at different zones of the control kidney were CO 23.2 (22.5–23.5), OSOM 24.5 (23.4–25.6), and ISOM 26.4 (25.8–27.7) ms. No significant differences in baseline T_2 were found between the stenotic and contralateral kidneys of RAS mice (Fig. 4b–d). After Mn^{2+} infusion, mild decreases in renal T_2 values were observed (Fig. 4b–d). Since the post-Mn^{2+} T_2 values were still much larger than the effective TE (4.8 ms), the condition in Eq. 4 was met, which justified the linear interpolation of M_0 images at different time points during Mn^{2+} infusion.

Dynamic MEMRI Study

Dynamic R_1 changes in CO, OSOM, ISOM, and IM of control, stenotic, and contralateral kidneys after saline injection are shown in Supporting Figure S1. No significant changes in R_1 through the wash-in and washout periods were observed, indicating negligible changes in renal perfusion during the 30-min dynamic imaging. Representative T_1 maps and changes in R_1 in control and RAS mice are shown in Fig. 5. At baseline, CO and OSOM in the stenotic kidneys showed elevated T_1 values (P=0.031 and 0.0075, respectively) compared to the control kidneys (Fig. 5c), possibly due to edema (21). In control kidneys, R_1 showed an approximately linear increase during Mn^{2+} infusion and reached a steady state during washout in CO and OSOM, but a slight decrease in ISOM (Fig. 5b). The OSOM (0.64 (0.61–0.69) s^{-1}) showed a larger increase in R_1 (Fig. 5d), compared to CO (0.53 (0.50–0.55) s^{-1}, P<0.0001) and ISOM (0.46 (0.44–0.54) s^{-1}, P<0.0001).

Compared to the control and contralateral kidneys, the stenotic kidneys showed slower increases in R_1 during Mn^{2+} infusion and lower steady-state R_1 values during washout (Fig. 5b). As a result, the changes in R_1 (ΔR_1, in s^{-1}) from baseline to post-Mn^{2+} infusion in the stenotic kidney (CO, 0.51(0.41–0.53); OSOM, 0.48 (0.38–0.56); ISOM, 0.43 (0.38–0.46); IM, 0.09 (0.07–0.09) s^{-1}) were significantly decreased compared to the control (CO, 0.53(0.50–0.55), P=0.0484; OSOM, 0.64 (0.61–0.69), P<0.0001; ISOM, 0.46 (0.44–0.54), P=0.0274; IM, 0.11 (0.10–0.21), P=0.0328) and contralateral (CO, 0.56(0.52–0.62), P=0.0067; OSOM, 0.67 (0.62–0.71), P=0.0001; ISOM, 0.54 (0.50–0.59), P=0.0007; IM, 0.13 (0.11–0.16), P=0.0189) kidneys (Fig. 5d). Interestingly, the largest decrease in R_1 was observed in OSOM (Fig. 5b&d), suggesting its highest vulnerability to ischemia.

In the contralateral kidneys, the time courses of R_1 (Fig. 5b) and ΔR_1 (Fig. 5d) in CO and OSOM showed no differences from the control kidneys. However, a slightly larger increase in the ISOM R_1 (Fig. 5b) led to a larger ΔR_1 (P=0.0378) compared to the control kidneys (Fig. 5d).

The ICP-MS-measured Mn concentration in mouse kidneys is shown in Fig. 6a. Consistent with the measured ΔR_1 in MEMRI, the stenotic kidneys (0.14 (0.13–0.15) mM) showed lower Mn concentration than the control (0.17 (0.16–0.19), P=0.0376) and contralateral (0.19 (0.18–0.19), P=0.0047) kidneys. The correlation between Mn concentration and ΔR_1 yielded a Mn^{2+} relaxivity of 2.77 $mM^{-1}s^{-1}$ in mouse kidneys at 16.4 T and 36°C (Fig. 6b). This in-vivo relaxivity was considerably smaller than the one measured in the phantom study

(2.77 vs. 6.16 $mM^{-1}s^{-1}$), possibly due to the temperature dependence of Mn^{2+} relaxivity (22, 23) or interactions with other molecules in vivo. Using this relaxivity, representative Mn concentration maps for control, stenotic, and contralateral kidneys at the end of washout were generated (Fig. 6c). Compared to the control and contralateral kidneys, the stenotic kidneys showed less Mn^{2+} uptake. Importantly, the Mn^{2+} uptake in OSOM was highest in both control and contralateral kidneys.

DISCUSSION

In this study, we first developed and validated a rapid multi-slice T_1 mapping method, MSRFSE, that allowed the measurement of T_1 in-mouse kidney at a temporal resolution of 1.43 min. Baseline T_1 values of CO, OSOM, ISOM, and IM in normal and RAS kidneys at 16.4 T were measured. The utility of MSRFSE in monitoring the dynamics of Mn^{2+}-induced T_1 changes during Mn^{2+} infusion and subsequent washout was then demonstrated in a dynamic MEMRI study using a low dose of $MnCl_2$. We found that the dynamic MEMRI by MSRFSE method successfully detected decreased cellular viability and discerned the regional renal responses to ischemia.

Manganese-enhanced MRI provides a tool for investigating cellular viability, because free Mn^{2+} can enter cells and retain for hours (7). Dynamic MEMRI offers the advantage of monitoring the kinetics of intracellular Mn^{2+} uptake, and has been used to successfully delineate infarcted myocardial tissues (14, 24) and detect subtle increase in cardiac L-type Ca^{2+} channel activity (16). Previously, it has been shown that a systemic administration of $MnCl_2$ led to comparable Mn^{2+} accumulation in heart and kidney of mice (12). Similar to the heart (8, 9), the ability of Mn^{2+} uptake and retention in kidney might be affected by its viability. Therefore, we sought to explore the ability of dynamic MEMRI to detect and delineate renal regional responses to ischemia in a mouse model of unilateral RAS, with the aid of a newly developed rapid T_1 mapping method, MSRFSE.

Compared to inversion recovery-based T_1 mapping methods, saturation recovery-based methods are faster but suffer from a small dynamic range. To achieve reliable T_1 fitting, high SNR and a small number of fitted parameters are desirable. In this study, we used fast spin echo readout with centric encoding to achieve high SNR (>80 in the M_0 image) and acquisition of the proton density image to limit the number of fitted parameters to two (saturation efficiency and T_1). As such, although only the initial portion of the recovery curve was sampled, the MSRFSE method can provide accurate and robust T_1 mapping. The major drawback of the FSE readout is the image blurring effect. We identified an ETL of 8 as providing a good balance between image resolution and acquisition time, were able to achieve a temporal resolution of 1.43 min for T_1 mapping in dynamic MEMRI.

Mn^{2+} at high doses may induce acute cardiac depression or even death (25, 26), but, the dose of $MnCl_2$ used in our study was much lower than that previously determined to be safe in mice (13, 16). Thuen et al. reported that direct intravitreal injection of $MnCl_2$ at doses between 150–300 nmol provided optimal contrast in the visual pathway of rats, and that higher doses caused retinal ganglion cell death and subsequent impaired clearance of Mn^{2+} from the vitreous (27). In our study, the dose of $MnCl_2$ injected through the tail vein was

800 nmol for a 25 g mouse. Given the systemic distribution of Mn^{2+}, the uptake of $MnCl_2$ in the renal pathway is presumably much less than 300 nmol (12). Therefore, the dose reaching the retinal ganglion cells with our dose is unknown, but likely much lower than that achieved using direct intravitreal injection. With this dose, T_1 in all renal zones showed more than a twofold decrease, whereas T_2 dropped by a much lower extent (<40%). Differential alterations in T_1 and T_2 have been attributed to binding of Mn^{2+} to macromolecules in vivo, which reduces its contact contribution to T_2 relaxation (12). We took advantage of this small change in T_2 to justify the linear interpolation of proton density images from pre- and post-contrast images.

Our MEMRI study showed robust Mn^{2+} uptake and retention in normal mouse kidneys. The mechanism for Mn^{2+} uptake in the kidney remains to be investigated, but might involve Mn^{2+} entry through voltage-gated Ca^{2+} channels, which are present in renal tubular cells (28, 29). The zinc transporters such as Zrt, Irt-related protein-8 and -14, and divalent metal transporter-1, may also provide passage for Mn^{2+} influx. Notably, these channels are primarily expressed in the S3 of proximal tubules located at the OSOM of mouse kidneys, which may well account for the marked Mn^{2+} uptake that we observed in this zone (30, 31). In addition, the densely packed mitochondria (32), which accumulates Mn^{2+} (33), and high metabolic rate (34) in the medullary thick ascending limb, may also account for the higher Mn^{2+} uptake in the OSOM. During washout, R_1 reached a steady state, suggesting retention of Mn^{2+} in renal tubular cells, possibly due to binding to macromolecules or uptake by mitochondria (2).

Decreased Mn^{2+} uptake was observed in the stenotic kidney, likely due to impaired tissue viability, leading to consistently lower tissue Mn levels, which were accentuated throughout the wash-in phase. Compared to the CO, ISOM, and IM, the OSOM showed the largest drop in Mn^{2+} uptake, consistent with its high susceptibility to ischemia. Indeed, we have previously shown a selective loss of OSOM cells in stenotic kidneys (21), possibly due to a higher susceptibility of this kidney zone to ischemia (35, 36). Our findings are consistent with previous studies, which showed that ischemia resulted in damage primarily in the corticomedullary border of the kidney in the outer medulla (37) and that prolonged ischemia extended damage to the inner medulla (38). Interestingly, the contralateral kidney ISOM showed elevated Mn^{2+} uptake, possibly induced by increased metabolic activity secondary to increased functional burden in the contralateral kidney.

There are several limitations to our study. First, an ETL of eight was associated with slight image blurring in the acquired images as a result of the T_2 decay during the FSE readout. Nevertheless, we were able to generate satisfactory T_1 maps, which successfully discerned different zones of mouse kidneys both at baseline as well as after contrast infusion. Second, the prerequisite for the linear interpolation of the M_0 images requires the post-contrast T_2 to be much larger than the effective echo time, a condition that was met with our current low Mn^{2+} dose. However, with larger Mn^{2+} doses, T_2 may decrease dramatically and the error from such interpolation may rise, resulting in inaccurate T_1 measurement during Mn^{2+} infusion. Third, due to the long echo train readout, the MSRFSE method may not be applicable to the fast beating heart. Moreover, the toxicity of free Mn^{2+} may limit the clinical applicability of MEMRI. Yet, the advent of manganese chelates (9, 23, 39), and possibly other future methods to alleviate the toxicity of manganese, may offer opportunities for such applications. Given that the main elimination route of Mn^{2+} is in the bile (2), the effect of altered renal function on its clearance in this study was likely modest.

In conclusion, we developed an MSRFSE method for rapid renal T_1 mapping at 16.4 T. Both in vitro and in vivo validation studies showed a good agreement in T_1 mapping between this method and the previously established MSRLL method. The application of MSRFSE in the dynamic MEMRI experiments in stenotic kidneys detected zone-specific responses of renal tissues to ischemia. Taken together, dynamic MEMRI by MSRFSE may provide a valuable experimental tool for noninvasive evaluation of renal viability.

Supplementary Material

Refer to Web version on PubMed Central for supplementary material.

Acknowledgments

This study was partly supported by National Institutes of Health Grants DK104273, DK102325, DK73608, and HL123160.

References

1. Silva AC, Lee JH, Aoki I, Koretsky AP. Manganese-enhanced magnetic resonance imaging (MEMRI): methodological and practical considerations. NMR Biomed. 2004; 17(8):532–43. [PubMed: 15617052]
2. Pan D, Schmieder AH, Wickline SA, Lanza GM. Manganese-based MRI contrast agents: past, present and future. Tetrahedron. 2011; 67(44):8431–44. [PubMed: 22043109]
3. Cory DA, Schwartzentruber DJ, Mock BH. Ingested manganese chloride as a contrast agent for magnetic resonance imaging. Magn Reson Imaging. 1987; 5(1):65–70. [PubMed: 3586874]
4. Nordhoy W, Anthonsen HW, Bruvold M, et al. Manganese ions as intracellular contrast agents: proton relaxation and calcium interactions in rat myocardium. NMR Biomed. 2003; 16(2):82–95. [PubMed: 12730949]
5. Wendland MF. Applications of manganese-enhanced magnetic resonance imaging (MEMRI) to imaging of the heart. NMR Biomed. 2004; 17(8):581–94. [PubMed: 15761947]
6. Bruvold M, Nordhoy W, Anthonsen HW, et al. Manganese-calcium interactions with contrast media for cardiac magnetic resonance imaging: a study of manganese chloride supplemented with calcium gluconate in isolated Guinea pig hearts. Invest Radiol. 2005; 40(3):117–25. [PubMed: 15714086]
7. Waghorn B, Yang Y, Baba A, et al. Assessing manganese efflux using SEA0400 and cardiac T1-mapping manganese-enhanced MRI in a murine model. NMR Biomed. 2009; 22(8):874–81. [PubMed: 19593760]
8. Dash R, Kim PJ, Matsuura Y, et al. Manganese-Enhanced Magnetic Resonance Imaging Enables In Vivo Confirmation of Peri-Infarct Restoration Following Stem Cell Therapy in a Porcine Ischemia-Reperfusion Model. J Am Heart Assoc. 2015; 4(7)
9. Skjold A, Amundsen BH, Wiseth R, et al. Manganese dipyridoxyl-diphosphate (MnDPDP) as a viability marker in patients with myocardial infarction. J Magn Reson Imaging. 2007; 26(3):720–7. [PubMed: 17729351]
10. Antkowiak PF, Tersey SA, Carter JD, et al. Noninvasive assessment of pancreatic beta-cell function in vivo with manganese-enhanced magnetic resonance imaging. Am J Physiol Endocrinol Metab. 2009; 296(3):E573–8. [PubMed: 19116376]
11. Yamada M, Gurney PT, Chung J, et al. Manganese-guided cellular MRI of human embryonic stem cell and human bone marrow stromal cell viability. Magn Reson Med. 2009; 62(4):1047–54. [PubMed: 19526508]

12. Kang YS, Gore JC. Studies of tissue NMR relaxation enhancement by manganese. Dose and time dependences. Invest Radiol. 1984; 19(5):399–407. [PubMed: 6511248]
13. Hu TC, Pautler RG, MacGowan GA, Koretsky AP. Manganese-enhanced MRI of mouse heart during changes in inotropy. Magn Reson Med. 2001; 46(5):884–90. [PubMed: 11675639]
14. Waghorn B, Edwards T, Yang Y, et al. Monitoring dynamic alterations in calcium homeostasis by T (1)-weighted and T (1)-mapping cardiac manganese-enhanced MRI in a murine myocardial infarction model. NMR Biomed. 2008; 21(10):1102–11. [PubMed: 18780285]
15. Chen Y, Payne K, Perara VS, et al. Inhibition of the sodium-calcium exchanger via SEA0400 altered manganese-induced T1 changes in isolated perfused rat hearts. NMR Biomed. 2012; 25(11):1280–5. [PubMed: 22434695]
16. Jiang K, Li W, Jiao S, et al. Rapid multislice T1 mapping of mouse myocardium: Application to quantification of manganese uptake in alpha-Dystrobrevin knockout mice. Magn Reson Med. 2015; 74(5):1370–9. [PubMed: 25408542]
17. Chuang KH, Koretsky A. Improved neuronal tract tracing using manganese enhanced magnetic resonance imaging with fast T(1) mapping. Magn Reson Med. 2006; 55(3):604–11. [PubMed: 16470592]
18. Li W, Griswold M, Yu X. Rapid T1 mapping of mouse myocardium with saturation recovery Look-Locker method. Magn Reson Med. 2010; 64(5):1296–303. [PubMed: 20632410]
19. Lee D, Han S, Cho H. Optimization of sparse phase encodings for variable repetition-delay turbo-spin echo (TSE) T1 measurements for preclinical applications. J Magn Reson. 2017; 274:57–64. [PubMed: 27886558]
20. Chen Y, Li W, Jiang K, et al. Rapid T2 mapping of mouse heart using the carr-purcell-meiboom-gill sequence and compressed sensing reconstruction. J Magn Reson Imaging. 2016; 44(2):375–82. [PubMed: 26854752]
21. Jiang K, Ferguson CM, Ebrahimi B, et al. Noninvasive Assessment of Renal Fibrosis with Magnetization Transfer MR Imaging: Validation and Evaluation in Murine Renal Artery Stenosis. Radiology. 2017; 283(1):77–86. [PubMed: 27697008]
22. Dwek, RA. Nuclear magnetic resonance (N.M.R.) in biochemistry : applications to enzyme systems. Oxford [England]: Clarendon Press; 1975.
23. Gale EM, Atanasova IP, Blasi F, et al. A Manganese Alternative to Gadolinium for MRI Contrast. J Am Chem Soc. 2015; 137(49):15548–57. [PubMed: 26588204]
24. Hu TC, Bao W, Lenhard SC, et al. Simultaneous assessment of left-ventricular infarction size, function and tissue viability in a murine model of myocardial infarction by cardiac manganese-enhanced magnetic resonance imaging (MEMRI). NMR Biomed. 2004; 17(8):620–6. [PubMed: 15761951]
25. Brurok H, Schjott J, Berg K, et al. Manganese and the heart: acute cardiodepression and myocardial accumulation of manganese. Acta Physiol Scand. 1997; 159(1):33–40. [PubMed: 9124068]
26. O’Neal SL, Zheng W. Manganese Toxicity Upon Overexposure: a Decade in Review. Curr Environ Health Rep. 2015; 2(3):315–28. [PubMed: 26231508]
27. Thuen M, Berry M, Pedersen TB, et al. Manganese-enhanced MRI of the rat visual pathway: acute neural toxicity, contrast enhancement, axon resolution, axonal transport, and clearance of Mn(2+). J Magn Reson Imaging. 2008; 28(4):855–65. [PubMed: 18821627]
28. Bozic M, Valdivielso JM. Calcium signaling in renal tubular cells. Adv Exp Med Biol. 2012; 740:933–44. [PubMed: 22453977]
29. Hayashi K, Wakino S, Sugano N, et al. Ca2+ channel subtypes and pharmacology in the kidney. Circ Res. 2007; 100(3):342–53. [PubMed: 17307972]
30. Himeno S, Yanagiya T, Fujishiro H. The role of zinc transporters in cadmium and manganese transport in mammalian cells. Biochimie. 2009; 91(10):1218–22. [PubMed: 19375483]
31. Fujishiro H, Yano Y, Takada Y, et al. Roles of ZIP8, ZIP14, and DMT1 in transport of cadmium and manganese in mouse kidney proximal tubule cells. Metallomics. 2012; 4(7):700–8. [PubMed: 22534978]
32. Eirin A, Woollard JR, Ferguson CM, et al. The metabolic syndrome induces early changes in the swine renal medullary mitochondria. Transl Res. 2017; 184:45–56. e9. [PubMed: 28363084]

33. Hunter DR, Komai H, Haworth RA, et al. Comparison of Ca2+, Sr2+, and Mn2+ fluxes in mitochondria of the perfused rat heart. Circ Res. 1980; 47(5):721–7. [PubMed: 6774832]
34. Epstein FH. Oxygen and renal metabolism. Kidney Int. 1997; 51(2):381–5. [PubMed: 9027710]
35. Munshi R, Hsu C, Himmelfarb J. Advances in understanding ischemic acute kidney injury. BMC Med. 2011; 9:11. [PubMed: 21288330]
36. Sutton TA, Fisher CJ, Molitoris BA. Microvascular endothelial injury and dysfunction during ischemic acute renal failure. Kidney Int. 2002; 62(5):1539–49. [PubMed: 12371954]
37. Venkatachalam MA, Bernard DB, Donohoe JF, Levinsky NG. Ischemic damage and repair in the rat proximal tubule: differences among the S1, S2, and S3 segments. Kidney Int. 1978; 14(1):31–49. [PubMed: 682423]
38. Basile DP, Donohoe D, Roethe K, Osborn JL. Renal ischemic injury results in permanent damage to peritubular capillaries and influences long-term function. Am J Physiol Renal Physiol. 2001; 281(5):F887–99. [PubMed: 11592947]
39. Storey P, Chen Q, Li W, et al. Magnetic resonance imaging of myocardial infarction using a manganese-based contrast agent (EVP 1001-1): preliminary results in a dog model. J Magn Reson Imaging. 2006; 23(2):228–34. [PubMed: 16416440]

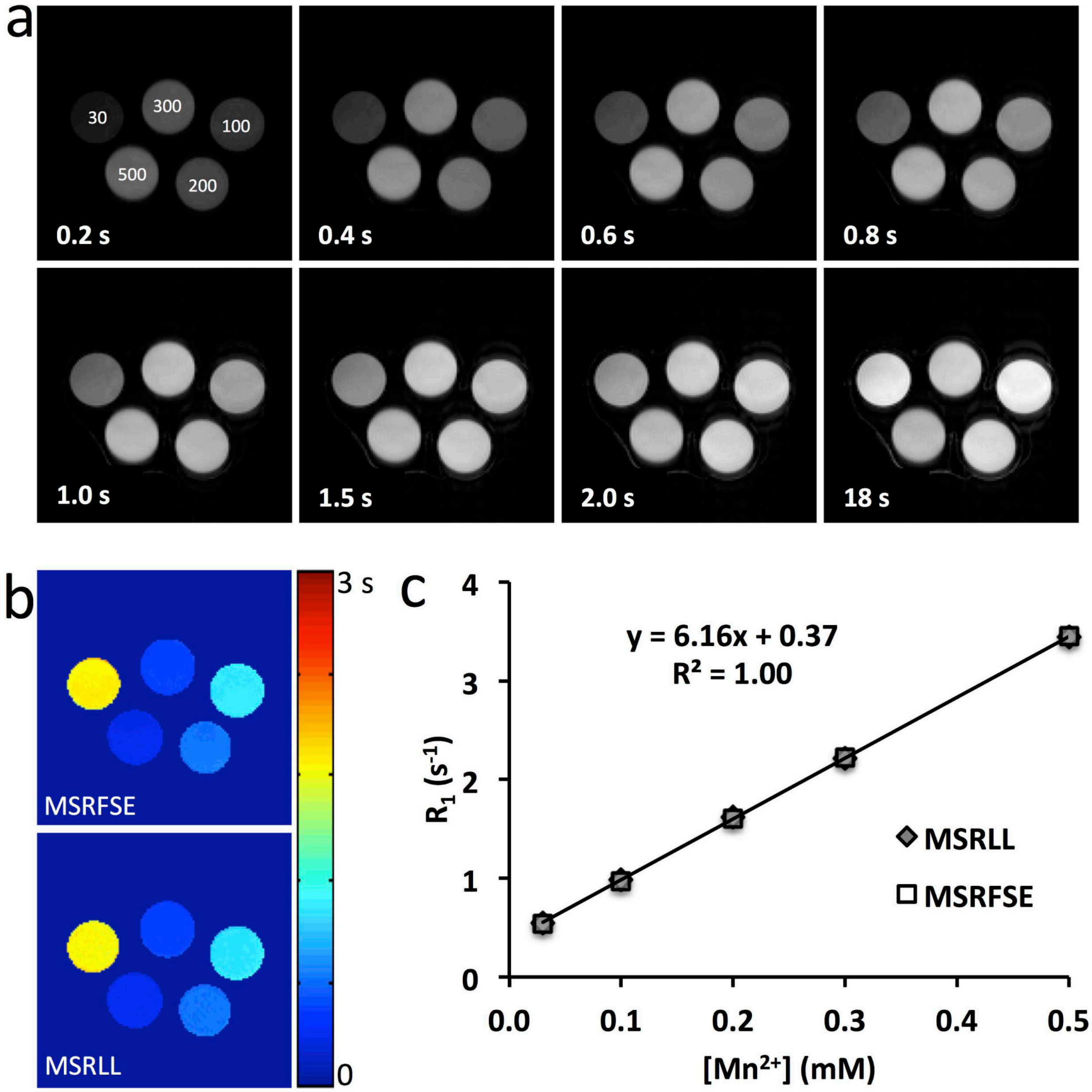

Figure 1. T_1 mapping of the $MnCl_2$ phantom

a. MSRFSE images acquired with varying TD in the $MnCl_2$ phantom (concentration (μM) was marked on the first image). **b.** T_1 maps measured by MSRFSE and MSRLL. **c.** Quantitative comparison of the T_1 measured by MSRLL and MSRFSE.

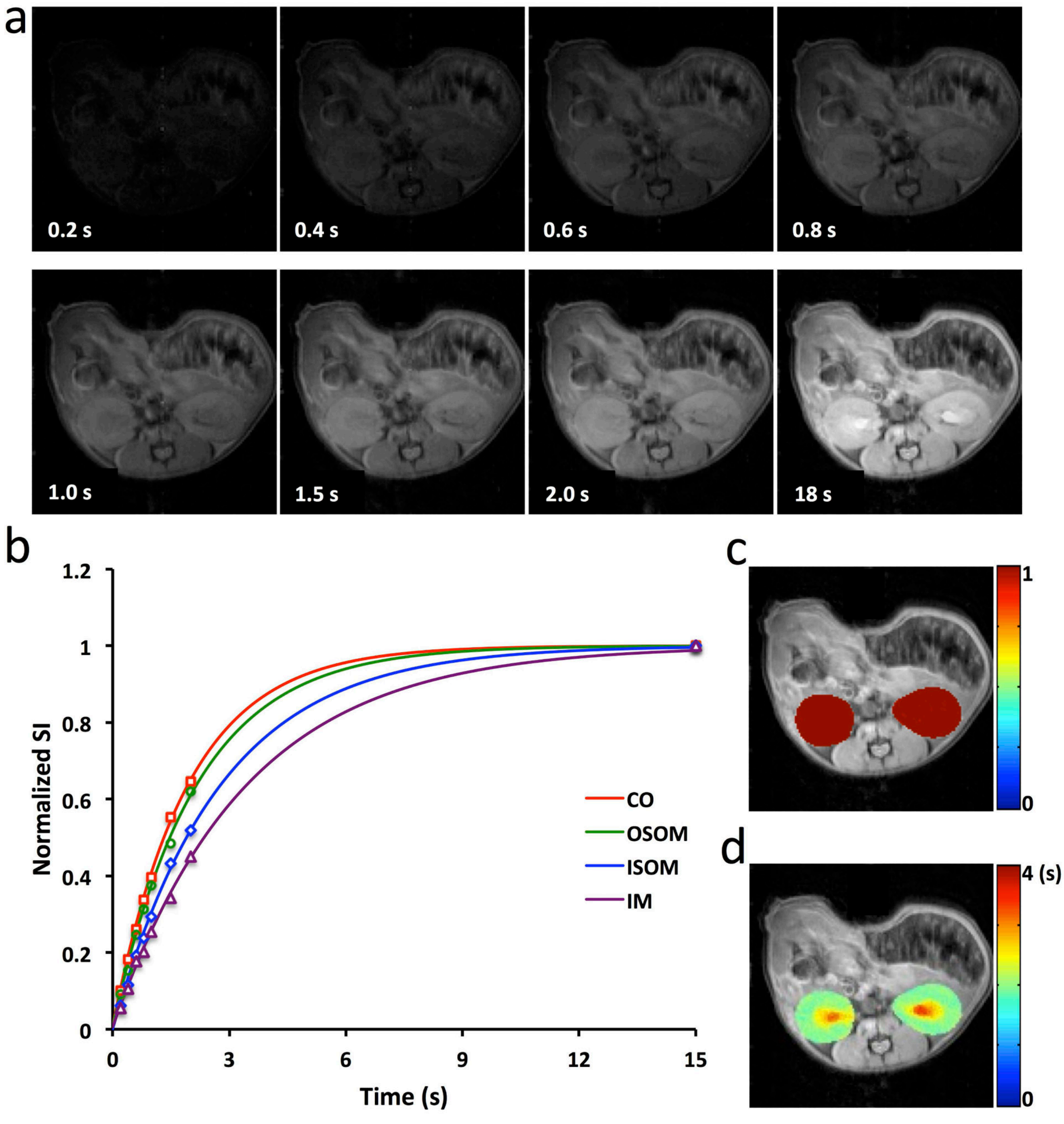

Figure 2. T_1 mapping of mouse kidneys

a. MSRFSE images acquired with varying TD. **b.** Representative experimental data and mono-exponentially fitted curve for one single pixel in CO, OSOM, ISOM, and IM, respectively. **c.** The fitted saturation efficiency map overlaid on the M_0 image. A good saturation of magnetization was achieved with averaged saturation efficiency larger than 99%. **d.** The fitted T_1 map overlaid on the M_0 image.

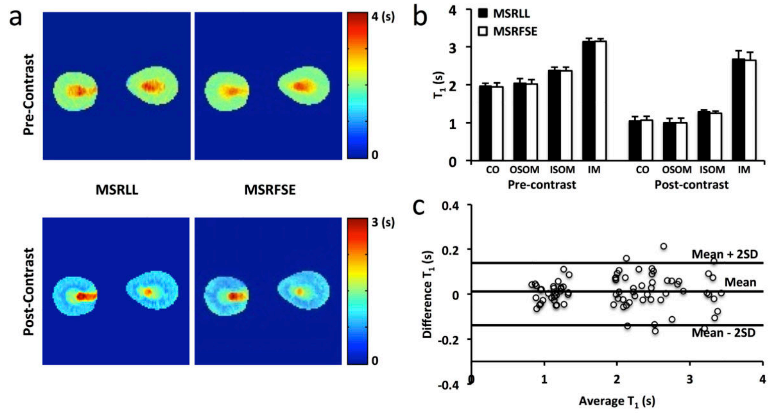

Figure 3. Validation of MSRFSE by MSRLL in vivo

a. Representative T_1 maps acquired at pre- and post-Mn^{2+} infusion by MSRLL and MSRFSE, respectively. **b.** Comparison of T_1 values quantified in CO, OSOM, ISOM, and IM by MSRLL and MSRFSE. **c.** Bland-Altman analysis of the measured T_1 values by both methods at pre- and post-Mn^{2+} infusion.

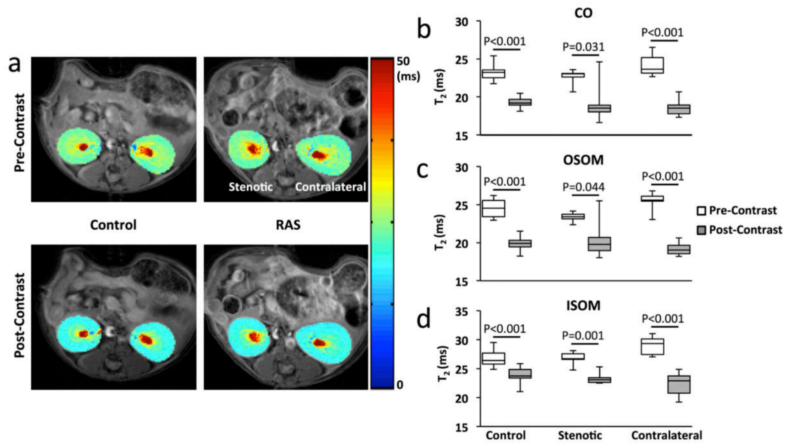

Figure 4. T_2 mapping at pre- and post-contrast

a. Representative T_2 maps acquired at pre- and post-Mn^{2+} infusion in control and RAS mice. **b–d.** Measured T_2 values in CO (**b**), OSOM (**c**), and ISOM (**d**) of control, stenotic, and contralateral kidneys at pre- and post-contrast.

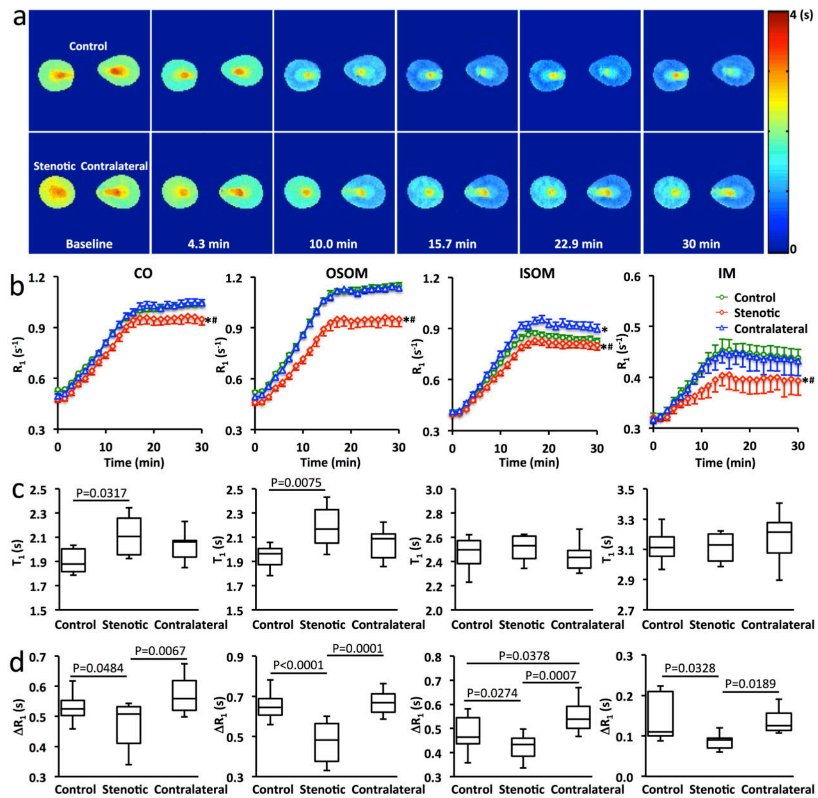

Figure 5. Dynamic MEMRI

a. Representative T_1 maps of the control, stenotic, and contralateral kidneys at baseline and 4.3, 10.0, 15.7, 22.9, and 30 min after the start of Mn^{2+} infusion. **b.** Quantified time courses of R_1 changes in CO, OSOM, ISOM, and IM of control, stenotic, and contralateral kidneys. Data expressed as mean±standard error. *P<0.05 compared to the control kidney; #P<0.05 compared to the contralateral kidney. **c&d.** The measured baseline T_1 values (**c**) and R_1 changes from baseline to post-contrast (**d**) in CO, OSOM, ISOM, and IM of control, stenotic, and contralateral kidneys.

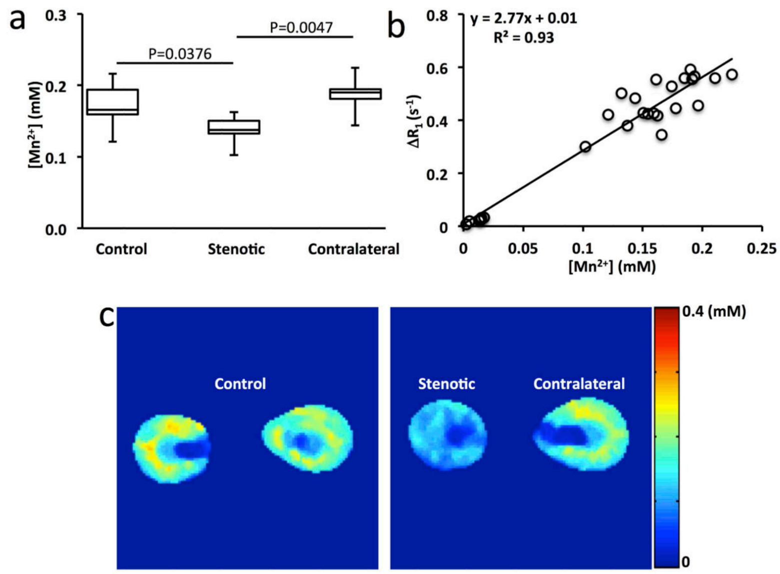

Figure 6. Measurement of Mn concentration in mouse kidneys

a. The Mn concentration in control, stenotic, and contralateral kidneys by ICP-MS. **b.** Correlation between Mn concentration and change in R_1 by MSRFSE. **c.** Representative Mn concentration maps of control, stenotic, and contralateral kidneys.

Table 1

Animal characteristics after 4 weeks of renal artery stenosis (RAS)

	Control (n=7)	**RAS (n=7)**	**P Value**
Body Weight (g)	26.6 ± 2.5	24.7 ± 1.9	0.173
Blood Pressure (mmHg)			
Systolic	122.9 ± 8.3	168.0 ± 19.1	<0.001
Diastolic	79.9 ± 5.8	125.9 ± 24.2	0.001
MAP	94.3 ± 5.7	139.9 ± 21.7	0.001

Data are means ± standard deviations. MAP=mean arterial pressure.